Engineered 3D Model of Cancer Stem Cell Enrichment and Chemoresistance

Maria R. Ward Rashidi[*,1], Pooja Mehta[*,1], Michael Bregenzer[†,1], Shreya Raghavan[*,1], Elyse M. Fleck[†], Eric N. Horst[†], Zainab Harissa[†], Visweswaran Ravikumar[‡], Samuel Brady[§], Andrea Bild[¶], Arvind Rao[†,#,**,††], Ronald J. Buckanovich[‡‡] and Geeta Mehta[*,†,††,§§]

[*]Department of Materials Science and Engineering, University of Michigan, Ann Arbor, MI, USA; [†]Department of Biomedical Engineering, University of Michigan, Ann Arbor, MI, USA; [‡]Department of Bioinformatics and Computational Biology, Division of Quantitative Sciences, The University of Texas MD Anderson Cancer Center, Houston, TX, USA; [§]Department of Pharmacology and Toxicology, University of Utah, Salt Lake City, UT, USA; [¶]Division of Molecular Pharmacology, Department of Medical Oncology and Therapeutics, City of Hope Cancer Institute, Duarte, CA, USA; [#]Department of Computational Medicine and Bioinformatics, Michigan Medicine, University of Michigan, Ann Arbor, MI, USA; [**]Department of Radiation Oncology, Michigan Medicine, University of Michigan, Ann Arbor, MI, USA; [††]Rogel Cancer Center, University of Michigan, Ann Arbor, MI, USA; [‡‡]Director of Ovarian Cancer Research, Magee Womens Research Institute, University of Pittsburgh, Pittsburgh, PA, USA; [§§]Macromolecular Science and Engineering, University of Michigan, Ann Arbor, MI, USA.

Abstract

Intraperitoneal dissemination of ovarian cancers is preceded by the development of chemoresistant tumors with malignant ascites. Despite the high levels of chemoresistance and relapse observed in ovarian cancers, there are no *in vitro* models to understand the development of chemoresistance *in situ*. *Method:* We describe a highly integrated approach to establish an *in vitro* model of chemoresistance and stemness in ovarian cancer, using the 3D hanging drop spheroid platform. The model was established by serially passaging non-adherent spheroids. At each passage, the effectiveness of the model was evaluated *via* measures of proliferation, response to treatment with cisplatin and a novel ALDH1A inhibitor. Concomitantly, the expression and tumor initiating capacity of cancer stem-like cells (CSCs) was analyzed. RNA-seq was used to establish gene signatures associated with the evolution of tumorigenicity, and chemoresistance. Lastly, a mathematical model was developed to predict the emergence of CSCs during serial passaging of ovarian cancer spheroids. *Results:* Our serial passage model demonstrated increased cellular proliferation, enriched CSCs, and emergence of a platinum resistant phenotype. *In vivo* tumor xenograft assays indicated that later passage spheroids were significantly more tumorigenic with higher CSCs, compared to early passage spheroids. RNA-seq revealed several gene signatures supporting the emergence of

https://doi.org/10.1016/j.neo.2019.06.005

CSCs, chemoresistance, and malignant phenotypes, with links to poor clinical prognosis. Our mathematical model predicted the emergence of CSC populations within serially passaged spheroids, concurring with experimentally observed data. *Conclusion:* Our integrated approach illustrates the utility of the serial passage spheroid model for examining the emergence and development of chemoresistance in ovarian cancer in a controllable and reproducible format.

Neoplasia (2019) 21, 822–836

Introduction

Of all the gynecological cancers, ovarian cancer has the highest mortality worldwide [1]. The first line of chemotherapy (combination of platinum and paclitaxel), although successful in ovarian cancer, often leads to recurrent chemoresistant disease [2–5]. Cancer stem-like cells (CSCs) are largely implicated for relapse of ovarian tumors, and the development of chemoresistance [6–11]. Therefore, chemoresistance and CSC-enrichment are recognized as major causes of failure for chemotherapy of ovarian tumors. Although advancement in genomic profiling has been successfully used to identify subtypes of ovarian cancer [12], its application to elucidating mechanisms of chemoresistance is still evolving and can be furthered with reliable and clinically relevant *in vitro* models of chemoresistance [3,5].

Several models have been developed to experimentally address and reproduce the complexity and heterogeneity of cancer and the pathobiologic mechanisms that underlie the poor survival of patients with ovarian cancers [3–5,13,14]. Given their relevance to tumor metastasis and relapse, models of *in situ* chemoresistance development are a primary target of study, for both fundamental understanding of cancer biology and the development of effective and targeted treatments. However, the currently available *in vitro* models are lacking in the ability to understand the development of chemoresistance *in situ*. Moreover, the existing studies rely only on cell lines in which platinum resistance is derived *in vitro*, the mechanisms of which may have little or no relevance in the clinical setting [5,15]. Additionally, these models lack a direct study of chemoresistance within a CSC-context, and therefore, *in vitro* models that incorporate CSCs' role in emergence of chemoresistance are critically important for developing biomarkers of chemoresistant disease, and for effectively targeting ovarian cancer. Currently available models for the study of CSCs rely on reprogramming, identifying side population or CSC populations using surface marker expression, selection of cells resistant to chemotherapy, modulation of oxygen tension, among others [16–19]. While these models derive CSCs with moderate success, CSCs are notoriously plastic in *in vitro* 2D monolayer culture conditions, making biological queries cumbersome.

Therefore, in this report, we present an engineered 3D ovarian cancer serial passage model that addresses the development of chemoresistance and the enhancement of CSC populations simultaneously. Previously, in ovarian and other cancers, serial passaging of spheroids *in vitro* and serial transplantation of tumor cells *in vivo* has been demonstrated to lead to increased tumor growth rates, and decreasing time to form tumors with increasing passage number [20,21]. We combined the power of serial passaging with 3D hanging drop array spheroids described by us extensively in previous reports [22–24], to create a novel engineered serially passaged 3D spheroid platform. This model combines the advantage of spheroids grown on a 3D platform, as previously described, over conventional 2D culture,

with the greater ease of an *in vitro* model compared to an *in vivo* model [22–26]. Moreover, compared to *in vivo* PDX serial passaging, our model is low cost, takes less time and can be applied to many more patient derived specimens. Furthermore, in contrast to our model, under same experimental conditions, serial passaging in 2D did not yield the same results.

Our model allows us to examine changing response to chemotherapy, along with a thorough investigation of proliferation, cell surface markers, and tumor initiating ability of serially passaged spheroids within a mouse xenograft in a reliably testable format. Using these experimental outcomes, we are able to inform our mathematical model describing the evolution of the CSC populations over the course of serial passaging ovarian cancer spheroids. By coupling our experimental data with a mathematical model, we can gain insights regarding CSC enrichment not otherwise possible, generate new hypotheses, and predict the outcome of experiments [27,28]. Given the correlation of drug resistance with CSC populations shown in our data and other reports [6,24], predicting CSC evolution allows us to infer the emergence of chemoresistance in a patient-specific manner within our model system. While there are many models of CSC population development [28–31], to our knowledge, none have been applied to a serial passaging platform to predict enrichment of CSCs. The unique strength of our math model is that it is informed by experimental data, including those obtained from patient samples. Moreover, the math model can be used to predict more complex environmental conditions that include hypoxia, stem cell plasticity, extracellular matrix physical–chemical properties, *etc.*

The innovation in our approach stems from the use of a powerful *in vitro* model to simultaneously assess the emergence of chemoresistance with CSC-enrichment, combined with gene sequencing queries that demonstrate the predictive and prognostic capability of this *in vitro* platform. Coupled with the mathematical model to predict CSC enrichment, this integrated platform has utility in guiding targeted therapies for ovarian cancers, and studying the underlying mechanisms of chemoresistant and recurrent disease.

Experimental Methods

Cell Culture

All reagents used in the experiments were purchased from Life Technologies (Carlsbad, CA), unless otherwise specified. The high grade serous ovarian adenocarcinoma cell line OVCAR3 was obtained from ATCC (Manassas, VA). Patient cells were recovered from primary patient ascites and primary or metastatic tumors after informed consent under approved IRB protocol, following

procedures established previously [6]. Briefly, primary patient malignant ascites infusions were centrifuged to recover a cell pellet, and red blood cells were lysed following manufacturer's protocol of a commercial ACK lysis buffer. Cells were obtained from primary or metastatic tumors using the tumor cell dissociation kit (Miltenyi Biotech, San Diego, CA) following manufacturer's protocols. Following 40 μm filtration to obtain single cell suspensions, cells were recovered by centrifugation and resuspended in a serum free medium. The patient samples utilized in this report were: tumor (Pt412, stage III, abdominal metastasis of high grade serous ovarian cancer) and ascites (Pt224, stage IV, platinum resistant ovarian adenocarcinoma).

OVCAR3 cells were cultured in 2D in 1640 RPMI supplemented with 10% fetal bovine serum and 1.5X antibiotics/antimycotics. Within the 3D hanging drop, OVCAR3 and Pt224 spheroids were cultured in serum-free medium, composed of 1:1 DMEM:Ham's F-12, supplemented with 1X B27 supplement without vitamin A, 1X MEM Non-Essential Amino Acids, 1X insulin-transferrin-selenium, 5 ng/mL Epidermal growth factor (EGF), and 5 ng/mL basic fibroblast growth factor (bFGF) [24,25]. Pt412 spheroids were plated in a serum free medium that was the same as above, except for 10 ng/ml EGF and bFGF. These cells were maintained in a humidified 37°C incubator with 5% carbon dioxide.

Generating Spheroids on the Hanging Drop Array

Spheroids were formed in hanging drop plates, purchased from XCentric Mold and Engineering (Clinton Twp, MI). For initial spheroid formation, cells were counted using a hemacytometer and diluted to contain 100 cells per 20 μL, and plated in 20 μL drops, following the procedure described previously [22–25]. Serum free medium (3 μL) was added to the spheroids every 2–3 days.

Serial Passaging of Ovarian Cancer Spheroids

At their first plating in the hanging drop array, the spheroids were labeled as passage 0 (P0). At each passage, spheroids were maintained for 7 days on the array. On day 7, spheroids were harvested by pipetting out the drop, and disassembled through mechanical disruption caused by repeated pipetting of the spheroid in quick succession followed by accutase treatment. These single cells were counted and plated on a new hanging drop plate with density of 100 cells per 20 μL to generate passage 1 (P1) spheroids. This entire process was repeated 5 more times, to reach a passage number of 6 (P6) by day 42. Phase images of the spheroids were collected using live cell microscopy on a calibrated phase contrast microscope (Olympus IX81, Japan equipped with ORCA R2 Cooled CCD camera and CellSens software) on days 1, 7, and 10 of spheroid growth for each passage. At least 3 representative images were collected for each hanging drop plate, and at least 5 serial passage experimental plates were prepared for each sample.

Drug Treatment of Serially Passaged Ovarian Cancer Spheroids

On day 7 of every passage, spheroids were treated with one of the following: 50 μM Cisplatin, 50 μM Compound 673A (a novel inhibitor that targets ALDH1A1, ALDH1A2, ALDH1A3; [32]), or no drug control (blank serum free medium). Three days after this treatment (day 10), phase images of the drug-treated and control spheroids were imaged and harvested for counting.

In order to examine proliferation and viability after drug treatment, alamarblue dye was used in a 1:10 dilution within the hanging drops, and fluorescence values were collected at 530 nm excitation and 590 nm emission within a microplate reader (Synergy HT, BioTek Instruments, Winooski, VT). Alamarblue from day 7 was normalized to day 1 for proliferation, and viability values from day 10 drug groups were normalized to non-drug treated values from day 10. Lastly, 10 spheroids were harvested from each drug treatment group, disassembled *via* mechanical disruption, and counted with trypan blue using a hemacytometer to assess viability and proliferation.

Fluorescence-activated Cell Sorting (FACS) on Serially Passaged Ovarian Cancer Spheroids

On day 7 of each passage, spheroids were collected and disassembled to single cells for FACS analysis according to previously established protocols [24,25]. The Aldefluor Kit was purchased from StemCell Technologies (Vancouver, BC, Canada), and used to analyze the activity of ALDH in viable cells within spheroids. CD133+ cells were detected using an Anti-CD133 antibody purchased from Miltenyi Biotec (San Diego, CA). Furthermore, spheroids at P0, P3, and P6 treated on day 7 with 50 μM Cisplatin, 50 μM Compound 673, or no drug treatment, were examined on day 10 using FACS.

FACS sorting for ALDH+ and ALDH- cells

OVCAR3 cells were sorted as ALDH+ and ALDH- cells, as described previously [24,25]. Briefly, cells were divided into equal volumes and concentrations across tubes, with at least 10,000 cells in each tube. Aldefluor assay was performed following the manufacturer's protocols, using DEAB as an established negative control, and activated Aldefluor reagent for positive staining of ALDH activity. Cells were incubated in the 37C incubator for 30 to 45 minutes, recovered by centrifugation, and resuspended in FACS buffer with 300 μmol/L 4′,6-diamidino-2-phenylindole (DAPI) to assess viability. Cells were processed through a flow cytometer, and forward and side scatter were used to isolate single cells, that were viable and DAPI negative. Gates were established using DEAB (less than 0.2% false positive), and stained tubes were used to sort for cells that represented ALDH+ and ALDH- populations.

RNA-seq

RNA was isolated from uncultured or cultured (P0, P3, or P6) spheroids derived from Pt224 and Pt412 using the Qiagen RNeasy Miniprep kit following manufacturer's protocol. RNA quality was verified using the Nanodrop, agarose Gel electrophoresis to test RNA degradation and potential contamination, as well as, RNA Integrity using Agilent 2100. After quality control, mRNA was enriched using oligo(dT) beads, and cDNA was synthesized by using mRNA template and random hexamer primers. cDNA library preparation was performed using a custom second-strand synthesis buffer (Illumina), and completed through size selection and PCR enrichment followed by quality control. Libraries were sequenced on the HiSeq 4000 (Illumina) by Novogene (Sacramento, CA).

The RNA-seq reads were aligned to the hg19 transcriptome using the pseudo-alignment tool Kallisto. The aligned reads were then imported and analyzed for differential expression using DESeq2 [33]. The transcript counts were summarized to gene-level counts using ensembl GRCh37 build using the biomaRt R package [34]. A

principle component analysis (PCA) plot of the samples was generated after variance-stabilizing transformation of the counts data.

For each patient, genes differentially expressed between the P0 and P6 passages at a false discovery rate (FDR) threshold of 0.1 and absolute $\log_2$ fold change threshold of 0.5 were identified. Heatmaps of the differentially expressed genes were plotted using the complex Heatmap package [35] in R after standardizing (centering and scaling) the expression data. Heatmaps of expression of 22 transcription factors (TFs) predicted to be activated in ovarian cancer stem cells in the literature are plotted to show the time-evolution of the serially passaged patient derived spheroids at P0, P3, or P6 [36].

Xenografts from Serially Passaged Ovarian Cancer Spheroids

NOD SCID gamma female mice were purchased from Jackson Laboratories (Bar Harbor, ME), and injected with ovarian cancer spheroids at a starting age of 8–12 weeks. Injections were prepared by carefully harvesting Pt224 and Pt412 spheroids using a pipette and supporting them within Growth-Factor-Reduced Matrigel from Corning (Corning, NY). Mice received subcutaneous injections of 1, 10 or 50 Pt224 spheroids generated from 100 cells after 7 days of growth, from spheroids at P0, P3, or P6 (n = 6 in each group) and 10 spheroids (100 cells/drop) at P0, P3 and P6 generated using Pt412 sample (n = 6 in each group). Tumor size was measured once weekly using calipers. Mice were euthanized after tumors reached 1500mm³ in volume, when tumors were then dissected, and placed within biopsy cassettes for histology, followed by Hematoxylin and Eosin staining.

Mathematical Modeling

Our two-compartment mathematical model was based on a simplistic set of differential equations proposed by Moliña et al. [29] and those proposed by Fornari et al. [28]. All simulations were performed in MATLAB version R2017b (Mathworks, Natick, MA, USA). Briefly, two equations were formulated; one describing change in the ALDH+ population, and the other describing changes in the ALDH- population (Supplementary Figure 1). Changes in the ALDH+ population are described by symmetric division, asymmetric division, symmetric differentiation, and death rates of ALDH+ cells. Contrarily, ALDH- cells are assumed to be capable of only symmetric division and death, and depend on asymmetric division and symmetric differentiation of ALDH+ cells. Rate constants with the units of cells per day were derived mainly from experimental data and supplemented with the literature. Briefly, the symmetric division rate of ALDH+ cells is chosen based on the value that minimizes the collective difference between simulated cells per spheroid at the end of P0 and P1 and the observed cells per spheroid at the end of P0 and P1 (Supplementary Table 1). The symmetric division rate of ALDH- cells was chosen to maintain an approximate ALDH+:ALDH- proliferation rate calculated from FACS data and cell counts at the end of P0 and P1. Cell death rate of ALDH+ and ALDH- cells were determined *via* FACS. The asymmetric division rate was determined from Tomasetti et al. [37], while the rate of symmetric differentiation by ALDH+ cells, has been found to be low through the observation of single cell divisions of ovarian cancer cell lines and primary samples, and is therefore taken to be 0 in this model [37,38] (Supplementary Table 2).

Data Analysis

All serial passages were repeated with at least 5 biological replicates, with n ≥ 10 for each replicate for alamarblue analysis, and 3 cell counts for trypan blue. Analysis of flow cytometry data was performed on Summit Software (Beckman Coulter, Brea, CA). At least 10,000 live cells were analyzed for each experimental condition and used to determine percentage of ALDH or CD133 positive cells. For xenografts, longitudinal tumor growth was compared between different groups (naïve Pt224 or P0, P3, P6 spheroids, naïve Pt412 or P0, P3, P6 spheroids) using repeated measures ANOVA techniques and/or mixed-effect longitudinal models. Tumor weights were compared between different groups and controls using a student's two-sample t-test. Statistical data was analyzed in Graphpad Prism 7.0 (www.graphpad.com, San Diego, CA). One-way ANOVA was performed where necessary, with secondary post-hoc analysis. All data is presented as mean ± standard error of the mean. Significance was considered for $P \le .05$. Asterisks on the figure panels and legends indicate statistical significance.

Results

Proliferation Increased Within the 3D Engineered Serial Passage Model

The 3D engineered model of stemness and chemoresistance was established by serial passaging of non-adherent ovarian cancer spheroids on the hanging drop array. In order to evaluate the effect of the model on cell proliferation, the kinetics of cell growth in the 3D suspension were evaluated at each passage. At every passage in the model, spheroids were initially seeded at 100 cells per spheroid. This consistency was also evaluated by checking cell viability on Day 1, and no significant differences were present (Supplementary Figure 2). Furthermore, all three patient derived cells and cell lines (OVCAR3, Pt224, Pt412) formed spheroids with tight boundaries at every passage by Day 1, just 1 day after initial seeding of the cells into the 3D hanging drop array (Figure 1). The fold-changes in alamarblue fluorescence after 7 days of growth compared to Day 1, increased with serial passaging.

The alamarblue results indicated a linear increase in proliferation for OVCAR3 spheroids as passage number increased (Figure 1, A and B). At P6, the fold increase in alamarblue fluorescence was 12.2 ± 2.3, as compared to the fold-increase at P1 of just 6.5 ± 3.3. Cell counts reaffirmed this increase in proliferation, with the number of cells per spheroid increasing two-fold from P1 to P6 (54 ± 8.4 to 118 ± 7.8, Figure 1B). Pt224 ascites cell proliferation also increased significantly with increasing serial passage, though to a lesser degree as compared to the OVCAR3 spheroids (Figure 1, D and E). The corresponding values of fold-change in proliferation indicate a 6.2 ± 1.7-fold increase at P0, compared to a 7.2 ± 1.2-fold increase at P6. Lastly, the Pt412 cell spheroids underwent an increase from 4.4 ± 0.97-fold proliferation at P3, to 6.7 ± 1.4-fold at P6, higher than the initial P0 value of 5.7 ± 1.6-fold. However, in Pt412 spheroids, drop in proliferation was observed in P3 (Figure 1, G and H). For all three ovarian cancer cell types and patient samples, the fold-change in proliferation at P6 was significantly higher than the proliferation at P0. These results demonstrate that the model caused increases in proliferation in all 3 ovarian cancer cell types.

Cancer Stem Cell Populations Were Enriched in Spheroids Within This 3D Engineered Serial Passage Model

In order to further examine the evolution of the CSC populations in our model, we quantified the ovarian CSCs expressing ALDH+ and CD133+ in the serially passaged spheroids. Given that chemoresistant CSCs prefer to form spheroids in suspension cultures, and can be enriched in such cultures, we assessed the effect of this model on the CSC subpopulation. Figure 2 shows the percentage of
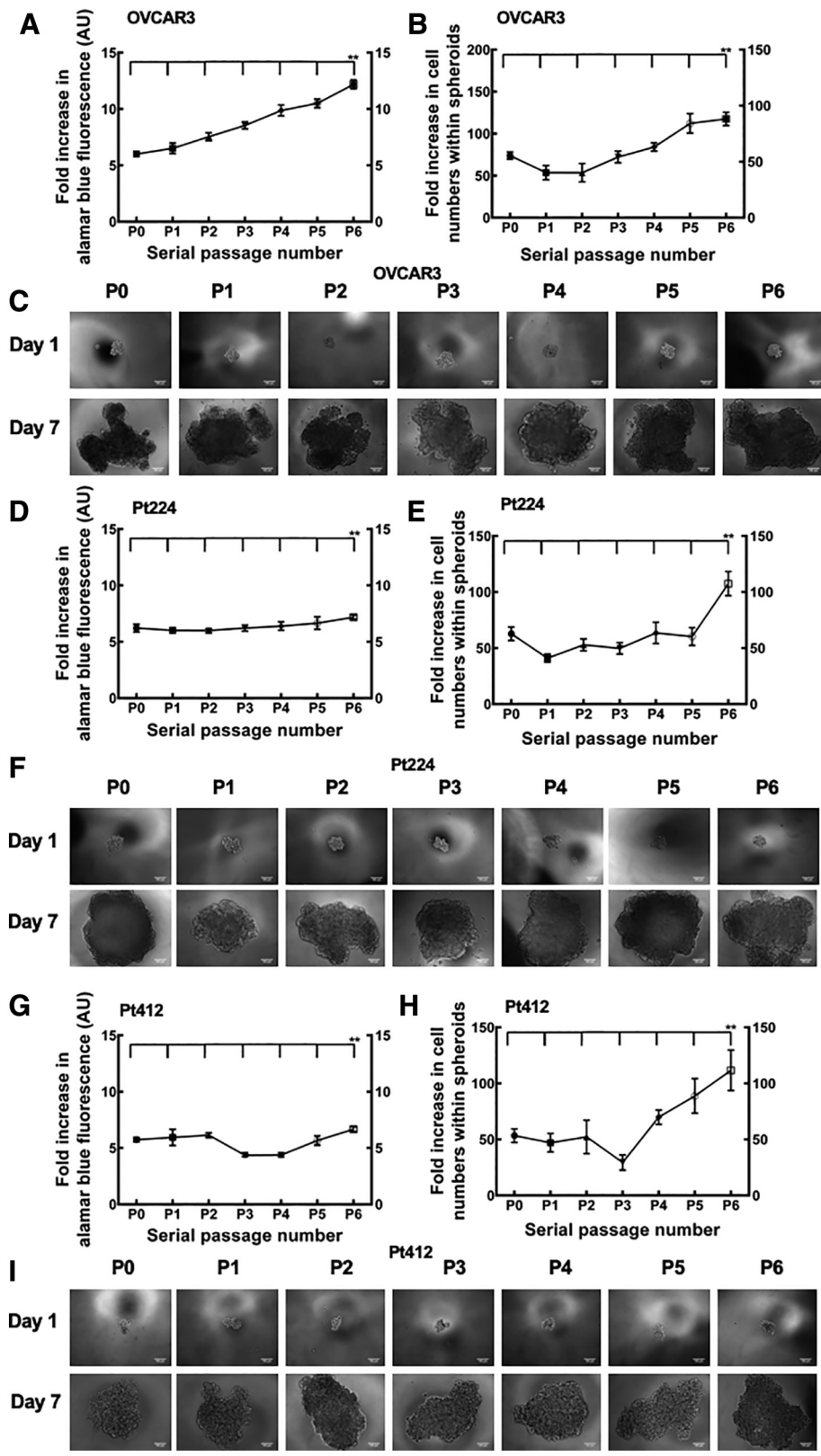
Figure 1. The 3D engineered serial passage hanging drop array model enhances proliferation in OVCAR3, Pt224, and Pt412OV spheroids initiated at 100 cells/drop. Fold increase in proliferation of **A)** OVCAR3, **D)** Pt224 cells, and **G)** Pt412 cells over 6 serial passages, based on alamarblue fluorescence at Day 7 normalized to Day 1 of each passage. Significant linear increase in proliferation as serial passage number increased was observed (n ≥ 6, with 150–200 spheroids formed for each experiment, *******P* ≪ .01, one-way ANOVA, horizontal line indicates significant differences between serial passages [P0-P6] in proliferation). Number of **B)** OVCAR3, **E)** Pt224, and **H)** Pt412 cells/spheroid quantified with trypan blue at Day 7 of each passage. Significant linear increase in proliferation is observed as spheroids are passaged serially (n ≥ 6, with 150–200 spheroids formed for each experiment, *******P* ≪ .01, one-way ANOVA, horizontal line indicates significant differences between serial passages [P0-P6] in proliferation). Representative phase contrast micrographs of **C)** OVCAR3, **F)** Pt224, and **I)** Pt412 spheroids at Day 1 and Day 7 at each passage. Scale bar = 100 μm.

total cells that are ALDH+ and CD133+ in OVCAR3, Pt224, and Pt412 respectively. From P0 to P6 in the OVCAR3 serially passaged spheroids, there was 5.6-fold increase of ALDH+ cells from P0 to P6 (from 2.28 ± 0.33 to 12.7 ± 2.21 percent), and a 2.5-fold increase in CD133+ cells (1.58 ± 0.46 to 3.97 ± 0.30 percent; Figure 2A). A significant increase in ALDH+ and CD133+ cells were observed in the Pt224 cells as well, with nearly a 5.1-fold increase in ALDH+ cells from P0 to P6 (1.63 ± 0.08 to 8.44 ± 0.26 percent), and a 1.5-fold increase in CD133+ cells (2.27 ± 0.31 to 3.44 ± 0.5 percent; Figure 2B).
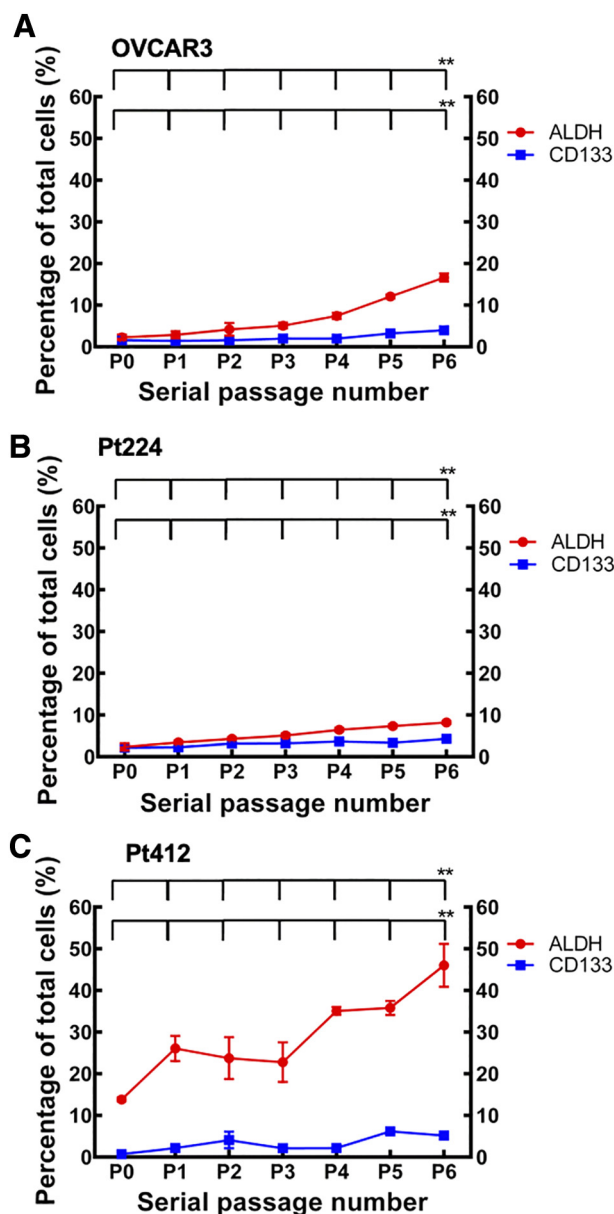
Although the ALDH+ cells in Pt412 spheroids started off relatively high, there was still a 2.4-fold increase in ALDH+ cells between P0 and P6 (18.7 ± 4.08 to 46.02 ± 5.16 percent; Figure 2C). The change in CD133+ population was especially high in Pt412 spheroids, with about a 7-fold increase between P0 and P6 (0.71 ± 0.09 to 5.18 ± 0.14 percent). The significant increase in ALDH+ and CD133+ cells in OVCAR3, Pt224, Pt412 spheroids serially passaged from P0 to P6 indicates that CSCs are enriched within this model. Moreover, serial passaging of the same cells in 2D was erratic, and did not show the same increase in ALDH+ and CD133+ populations as we observed within the spheroids.

Serially Passaged Spheroids in the 3D Engineered Model Exhibited Resistance to Cisplatin and Sensitivity to ALDH Inhibitor

After confirming that the CSCs were enriched in spheroids from P0 to P6, we hypothesized that resistance to cisplatin would also be observed as passage number increased within this model, and thus investigated the effectiveness of the model to enhance chemoresistance. Notably, there was an initial resistance to cisplatin in P0 following the first formation of spheroids in OVCAR3 that decreased upon passage to P1 (38% ± 2.23 viability in P0 to 27.3% ± 2.10 in P1). As hypothesized, when the spheroids were serially passaged from P1 to P6, this resistance to cisplatin increased (Figure 3). The viability of OVCAR3 spheroids fell to 27.3% ± 2.09 with cisplatin treatment at P1, and rose to 61.3% ± 2.36 at P6 (Figure 3A, C). Pt224 and Pt412 cell spheroids reacted in a similar manner as OVCAR3 spheroids, with cell viability values at P1 of 27.7% ± 1.23 and 46.9% ± 6 respectively following 50 µM cisplatin treatment, and 42.6% ± 3.19 and 69% ± 2.16 at P6 respectively (Figure 3, D, F, G, I).

Given that ALDH percentage increased with serially passaging, the spheroids were treated with 50 µM of Compound 673A, an ALDH inhibitor [32]. Cell viability in OVCAR3 spheroids dropped from 85.7% ± 2.6 at P1 to 69.8% ± 2.84 at P6 following treatment with the inhibitor (Figure 3B, C). An increase in sensitivity to Compound 673A resulted in cell viabilities of 98.2% ± 2.17 and 84.8% ± 2.63 at P1 and 63.3% ± 4.1 and 66.8% ± 3 at P6 of Pt224 and Pt412, respectively (Figure 3, E, F, H, I). These data corroborate increasing levels of CSCs in the spheroids as serial passage increased in this model. These data are consistent with our previous observations of ALDH inhibitor significantly reducing the viability of various patient derived CSC spheroids [24]. Serially passaging spheroids in the hanging drop array caused the emergence of resistance to cisplatin and increased sensitivity to the ALDH inhibitor.

ALDH Expression in Viable Cells Decreased Following Drug Treatment of Spheroids

Further, we sought to quantify the changes in the CSC population after treatment with cisplatin or ALDH inhibitor that occur within this model. Thus, we analyzed the ALDH activity in viable cells after these treatments. The percentages of ALDH+ cells in spheroids treated with 50 µM Cisplatin or 50 µM Compound 673A decreased compared to the controls. The ALDH+ population increased significantly with increased serial passage number (Figure 4). However, treatment with cisplatin decreased the levels of ALDH+ cells, with the exception of P0 for OVCAR3 and Pt224 spheroids. The greatest fold difference between control and drug treatment was clear in P6 spheroids. The decrease in ALDH+ cells was most drastic following treatment with the ALDH inhibitor.

Figure 2. This serial passage model increased populations of ALDH + and CD133+ cells. Percentage of ALDH+ and CD133+ populations in **A)** OVCAR3, **B)** Pt224, and **C)** Pt412 spheroids quantified from flow cytometry. Significant linear increase in both ALDH+ and CD133+ populations from P0 - P6 (n ≥ 4, with 150–200 spheroids formed for each experiment, **P ≪ .01, one-way ANOVA, top horizontal line indicates significant differences between serial passages [P0-P6] in ALDH, and the bottom line indicates differences in CD133).
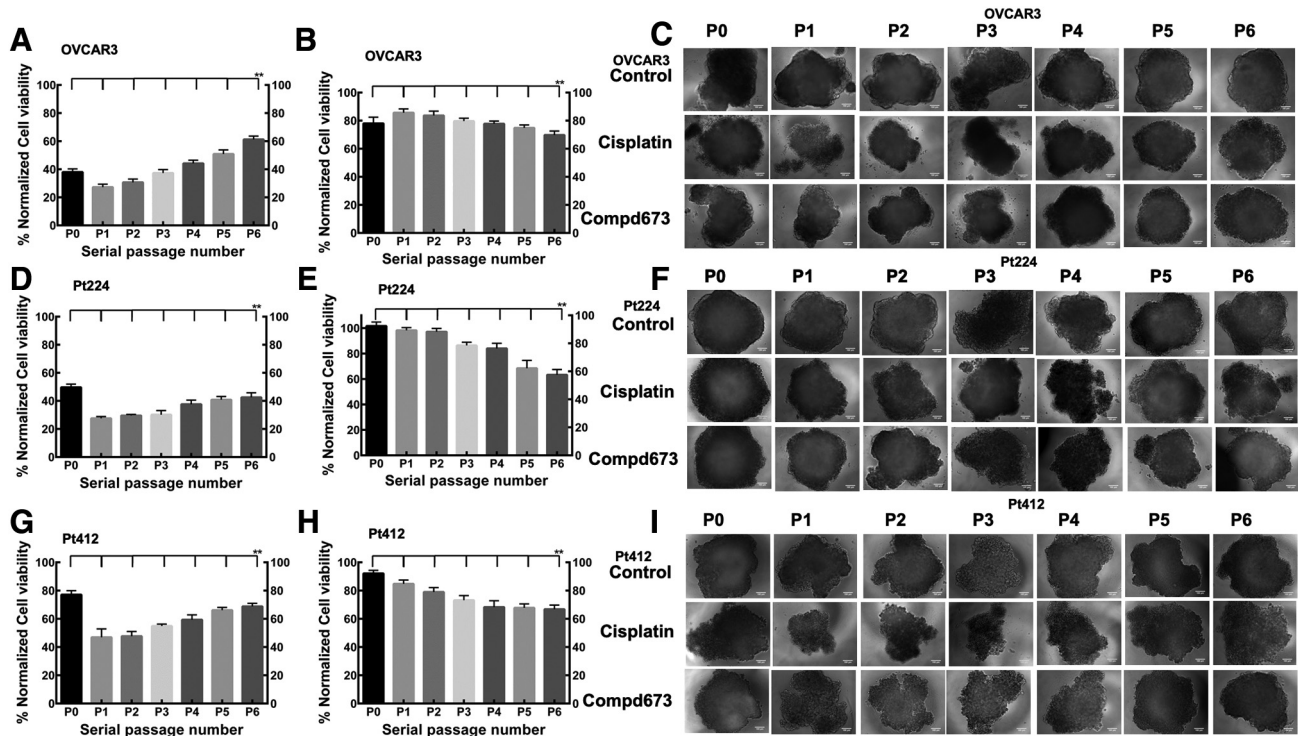
Figure 3. Resistance to cisplatin and sensitivity to ALDH inhibitor Compound 673 increase within this model. Percent viability of **A)** OVCAR3, **D)** Pt224, and **G)** Pt412 spheroids 3 days following treatment with 50 μM Cisplatin. Significant increase in cell viability over serial passage was observed (n $\geq$ 6, with 150–200 spheroids formed for each experiment per treatment group, **$P \ll .01$, one-way ANOVA, horizontal line indicates significant differences between serial passages (P0-P6) in cell viability after cisplatin treatment). Percent viability of **B)** OVCAR3, **E)** Pt224, and **H)** Pt412 spheroids 3 days following treatment with 50 μM of novel ALDH inhibitor Compound 673. Significant decrease in cell viability over serial passage was observed (n $\geq$ 6, with 150–200 spheroids formed for each experiment per treatment group, **$P \ll .01$, one-way ANOVA, horizontal line indicates significant differences between serial passages (P0-P6) in cell viability after Compound 673 treatment). Representative phase contrast micrographs of **C)** OVCAR3, **F)** Pt224, and **I)** Pt412 spheroids at Day 10, following 3 days of treatment. Scale bar = 100 μm.

Spheroids From the Serial Passage 3D Engineered Model Initiated Ovarian Tumors In Vivo, With Later Passage Spheroids Exhibiting Higher Tumorigenicity Than Early Passage Spheroids

After confirming that our model enriched the ALDH+ population and increased chemoresistance, we observed how tumor growth could be impacted by enrichment in CSCs and chemoresistance within this model. This was done by subcutaneously injecting a limiting number of spheroids or 2D grown cells (1 million cells) as positive control into the flanks of NSG mice (Figure 5, A and C). Tumorigenicity increased with serial passaging among tumors initiated from Pt224 P0, P3, or P6 spheroids. A similar trend was observed in tumors initiated from P6 and P3 spheroids as compared to P0 spheroids in mice injected with Pt412 derived spheroids (Figure 5B, Supplementary Figure 3). Following injection of 50 Pt224 spheroids, tumor growth from P6 spheroids was detectable as early as 2 weeks, with complete initiation of tumors from P3 and P6 spheroids by week 4 following injection. P0 spheroids completely initiated tumors by week 5. One million Pt224 cells from 2D culture-initiated tumors by week 4. Tumors from 2D cells reached the final tumor volume of 1500 mm^3 before the other tumor groups formed from 50 spheroids (Figure 5A). Following injection of 10 Pt224 spheroids, P6 spheroids had 100% initiation by week 4, and tumors from P3 spheroids achieved 100% initiation by week 5, with tumors from P0 spheroids initiated 100% by week 7 (Supplementary Figure 3). Similarly, after the injection of 4 spheroids, those from P6 initiated 100% tumors by

week 4, meanwhile the lower passage spheroids did not initiate tumors before week 6. Additionally, when just one Pt224 spheroid was injected, P0 spheroids did not form tumors through 15 weeks of observation, though both P6 and P3 spheroids were able to form tumors, with P6 tumors initiating 3 weeks prior to P3 spheroids. This differential tumor initiation also corresponded with differential time-points for reaching final tumor volume, with tumors from P6 spheroids reaching the endpoint before P3 spheroids, which reached the endpoint before P0 spheroids. In mice administered with 10 Pt412 derived spheroids, P0, P3 and P6 passages initiated tumors by week 2, but P6 reached the tumor volume endpoint earlier than the P0 and P3 passages, indicating a higher number of tumor initiating stem cells and higher tumorigenicity in P6. These results highlight the relevance of the serial passage model in modulating the tumor aggressiveness and accelerating rate of tumor formation in later passage spheroids.

Additionally, we examined the role of later passage spheroids in inducing larger tumor load and faster initiation using extreme limiting dilution analysis (ELDA) [34] (Figure 5, D–G, Supplementary Table S3). The fitted model displayed vastly different tumorigenicity and CSCs in the three groups. Specifically, in case of Pt224, the CSC frequencies in P6 increased to 1 in 0.6, from 1 in 28.5 at P3, and from 1 in 62 for P0 spheroids (Figure 5, D, F). Meanwhile for patient metastasis derived Pt412 sample, CSC frequency was estimated as 1 CSC per cell at P6, 1 CSC in 45 cells at P3, and 1 CSC in 92 cells at P0, which were significantly higher
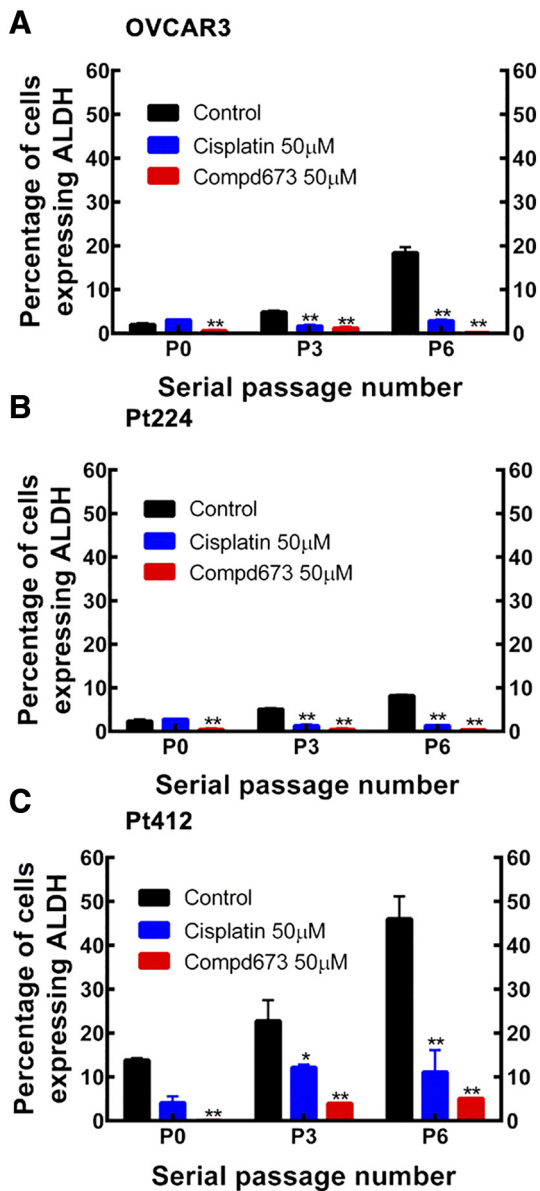
Figure 4. Population of ALDH+ cells decreases after treatment with Cisplatin and ALDH inhibitor Compound 673A. Percent of ALDH+ cells in **A)** OVCAR3, **B)** Pt224, and **C)** Pt412 spheroids following treatment with 50 μM Cisplatin, 50 μM ALDH inhibitor Compound 673, or spheroid serum free medium. Significant difference between control and drug treatment in all cases (n $\geq$ 4, with 150–200 spheroids formed for each experiment per treatment group, **$P \ll .01$, *$P \ll .05$, one-way ANOVA).

than CSC frequencies in patient ascites Pt224 spheroids. Therefore, Pt 412 demonstrated highly enriched cancer stem cell population in P6, as compared to P3 and P0 (Figure 5, E, G). These findings underline the role of serial passaging in enriching and maintaining CSCs [35].

Spheroids Initiated With ALDH+ Had Greater Proliferation Compared to ALDH- cells

Knowing that the serial passage hanging drop array model induced an increase in the percentage of ALDH expressing cells at later passages, we quantified the differences in the proliferation rates between spheroids initiated with ALDH+ and ALDH- cells. Spheroids initiated with ALDH+ cells had greater fold-changes in proliferation than ALDH- cells (Figure 6). Based on alamarblue fluorescence, a significant difference in proliferation was observed after a week of growth; with about a 5-fold difference in ALDH+ cells to near a 3-fold difference in ALDH- cells (Figure 6B). Moreover, there was a significantly higher percentage of cells expressing Ki67+ cells in the ALDH+ cells initiated spheroids compared to the ALDH- group (Figure 6C). This provides evidence that our model may be increasing the ALDH+ population over serial passage, and thereby causing the increase in proliferation that was observed.

RNA Sequencing Reveals Stemness, Tumorigenic and Chemoresistance Signatures Through In Vitro Passaging

Using RNA sequencing, we assessed genome-wide changes to RNA synthesis and stability in Pt412 and Pt224 CSC spheroids that underwent early (P0), middle (P3), or late (P6) serial passaging in the 3D model. Generation of a PCA plot from our gene-expression data shows a clear difference in gene signature between each patient sample (Figure 7A). Similarly, we observed a definitive trend showing changes in gene signature within each patient sample with serial passaging. This trend was also evident in Pt224 and Pt412 heatmaps showing significantly up- and down-regulated genes for each patient sample across P0, P3, and P6 spheroids (Figure 7B).

Of the significantly up-regulated genes for Pt224 (553 genes) and Pt412 (507 genes), a total of 142 genes were commonly upregulated in both patient samples. From these 142 genes, we identified and binned 9 of the most highly upregulated genes associated with stemness (*WLS* [39,40], *ALDH1A1* [41,42], *BMP2* [38,43], *RSPO3* [44,45]), tumorigenicity (*MAGEB2* [46,47], *BMP2* [38], *EFNB2* [48], *SERPINE2* [49–53], *HHIP* [54–56], *PTGS2* [57–60]), and chemoresistance (*WLS* [39,40,61], *ALDH1A1* [62,63], *BMP2* [38], *PTGS2* [57,64]) based on the literature (Figure 7, C, D). The upregulation of these genes between P0 and P6 for both patient samples was subsequently confirmed with qRT-PCR. While qRT-PCR confirmed the upregulation of all binned genes, ALDH1A1 was among the top two upregulated genes in both patient samples regardless of quantification metric (Figure 7D, E). Further analysis of 17 transcription factors previously associated with ovarian CSCs indicated that *FOXA1* and *LEF1* are significantly upregulated between P0 and P6 spheroids generated from Pt412 cells with the thresholds used in our analysis (Figure 7F) [36].

Mathematical Modeling Strongly Predicts Emergence of Cancer Stem Cell Populations, and Tumorigenicity Within Serially Passaged Spheroids

To further validate our experimental findings, and enhance the utility of our model as a predictive and prognostic tool, we developed a mathematical model describing the emergence of ALDH+ populations across 6 passages. In simulating the growth of a spheroid over 7 days for the OVCAR3 cell line (Figure 8A), as well as Pt224 (Figure 8B) and Pt412 cells (Figure 8C), we corroborate our experimental findings of increased proliferation in later passages. Spheroids formed from the Pt412 metastatic sample were predicted to exhibit the greatest increase in proliferation (1.19-fold simulated P0-P6 increase *vs.* 2.1-fold experimental P0-P6 increase) compared to the OVCAR3 cell line (1.084-fold simulated P0-P6 increase *vs.* 1.6-fold experimental P0-P6 increase) and the Pt224 ascites sample (1.083-
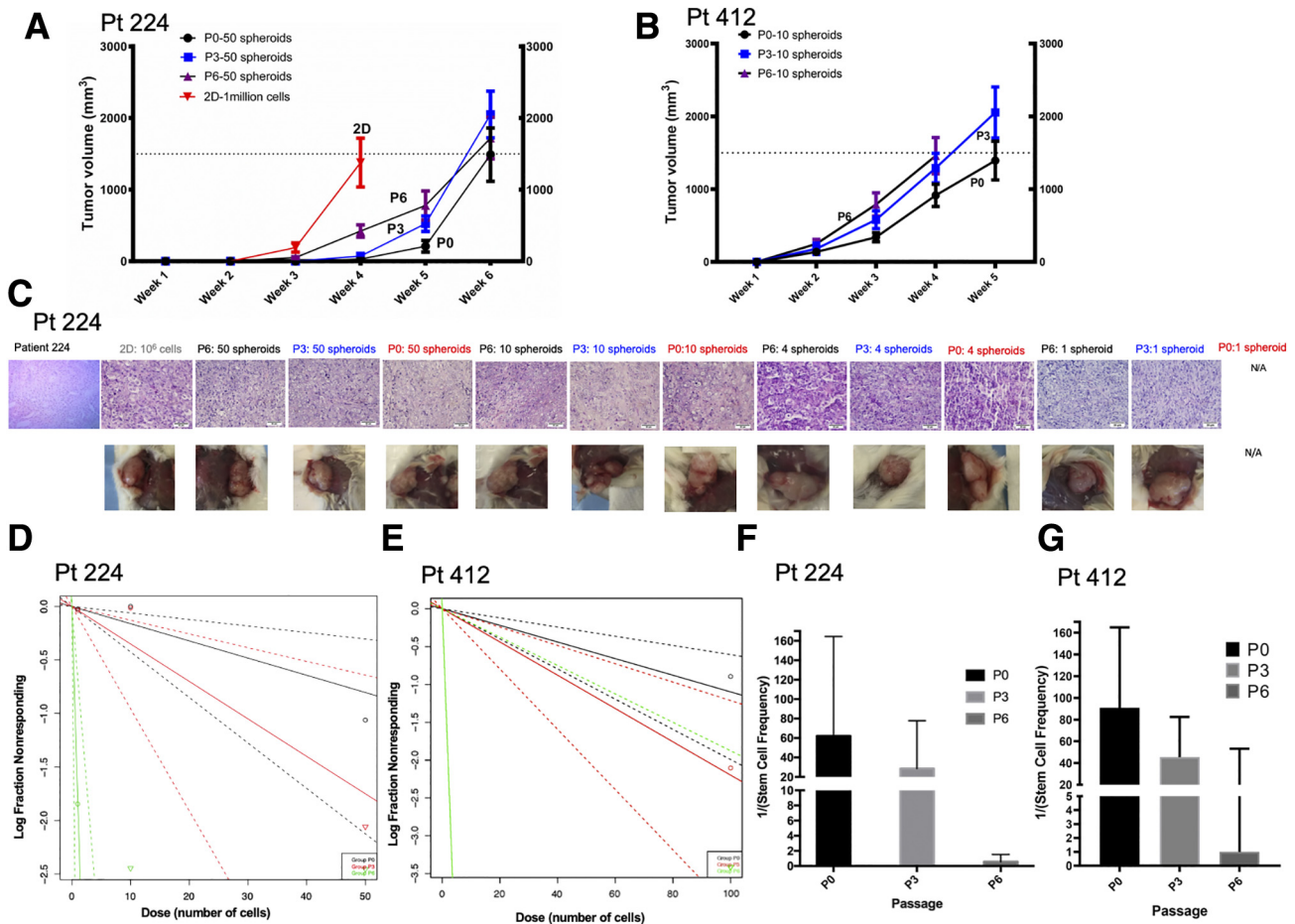
Figure 5. Spheroids from higher serial passage number within this model are more tumorigenic in NSG mice. **A)** For Pt224, tumor volume as a function of time for 50 spheroid/s (n = 6 in each group). Fifty spheroids from P0, P3, and P6 all reached the endpoint of 1500 mm^3 by week 6, and 1 million 2D grown cells reached endpoint by week 4. **B)** For Pt412, tumor volume as a function of time for 10 spheroids (n = 6 in each group). 10, 100 cell spheroids from P0 and P3 reached the endpoint of 1500 mm^3 by week 5, while P6 group reached end point by week 4. **C)** Macroscopic pictures and photomicrographs of hematoxylin and eosin images of naïve patient tumor and xenografts observed in NSG mice with subcutaneous injections of spheroids or 2D grown cells. Scale bar = 50 μm. **D)** Plot for Pt224 of the log fraction of mice bearing no tumors in 4 weeks (Log fraction nonresponding) as a function of the number of spheroids injected in NSG mice at that serial passage (Dose). The slope of the line: log-active cell fraction; dotted lines: 95% confidence interval; down-pointing triangle: cell dose with 0 non-xenografted mice. The more vertical the line, the higher the percentage of stem cells in that passage (n = 6, ****$P \ll .0001$). **E)** Plot for Pt412 of the log fraction of mice bearing no tumors in 4 weeks (Log fraction nonresponding) as a function of the number of spheroids injected in NSG mice at that serial passage (Dose). The slope of the line: log-active cell fraction; dotted lines: 95% confidence interval; down-pointing triangle: cell dose with 0 non-xenografted mice. The more vertical the line, the higher the percentage of stem cells in that passage (n = 6, ****$P \ll .0001$). **F)** Inverse of frequency of stem cells as determined by Extreme Limiting Dilution Analysis (ELDA) between different passages for Pt224. Lower number indicates higher fraction of cancer stem cells in P6, compared to P3 or P0 (n = 6, ****$P \ll .0001$). **G)** Inverse of frequency of stem cells as determined by Extreme Limiting Dilution Analysis (ELDA) between different passages for Pt 412. Lower number indicates higher fraction of cancer stem cells in P6, compared to P3 or P0 (n = 6, ****$P \ll .0001$).

fold simulated P0-P6 increase *vs* 1.7-fold experimental P0-P6 increase). As expected, this increase in proliferation corresponded with increased ALDH+ percentages, with Pt412 spheroids exhibiting highest ALDH+ levels (35.61% simulated *vs* 46±5.2% experimental) after 6 passages (Figure 8*G*), followed by OVCAR3 spheroids (9.78% simulated *vs* 12.1±2.2% experimental) (Figure 8*E*) and lastly Pt224 spheroids (8.65% simulated *vs* 8.4±0.26%) (Figure 8*F*). These findings mirrored our experimental data confirming the ability of our model to reproduce biological trends. Interestingly, the model also predicts a plateau in cells per spheroid and ALDH+ cells within spheroids of each patient sample, which could not be perceived from our experimental data. This is especially evident when the model is

used to simulate 20 passages, indicating that Pt412 cells per spheroid begins to plateau around passage 9 (9206 cells/spheroid), while the increased percentage of ALDH+ cells is predicted to plateau around passage 11 (~38.0%). On the other hand, Pt224 and OVCAR3 spheroids are predicted to plateau in cells per spheroid around passage 18 (5506 and 7160 cells/spheroid respectively) and in percentage of ALDH+ cells around passage 20 (~30.6% and ~28.7% respectively; Figure 8*D, H*).

Discussion

Ovarian CSCs are putative mediators of chemoresistance and recurrent disease, escaping conventional chemotherapy and
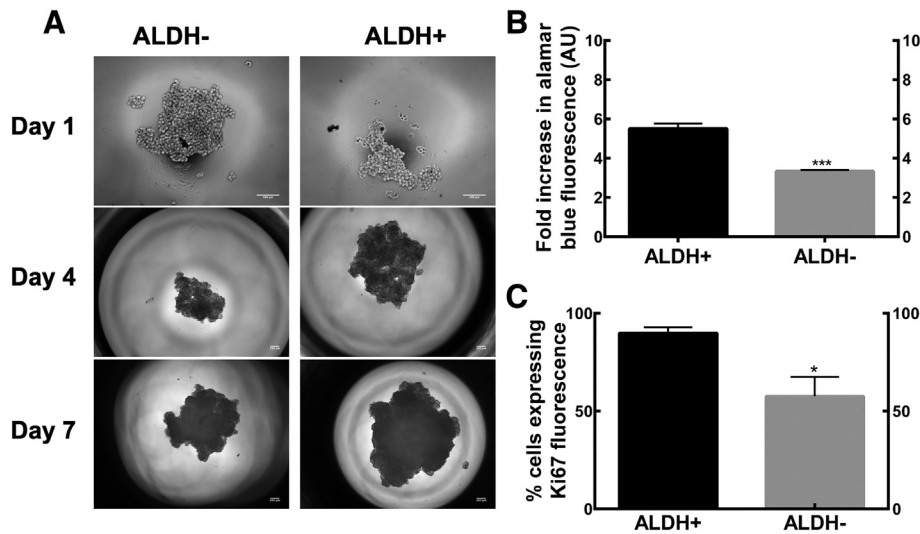
Figure 6. ALDH+ OVCAR3 spheroids have higher proliferation than ALDH- spheroids. **A)** Representative phase contrast micrographs of ALDH+ and ALDH- OVCAR3 spheroids at Days 1, 4, and 7 (Scale bar = 100 μm). **B)** Fold increase in proliferation of ALDH+ and ALDH- OVCAR3 cells, based on alamarblue fluorescence at Day 7 normalized to Day 1 of each passage. **C)** Percent of cells expressing Ki67 higher in ALDH+ spheroids, quantified *via* flow cytometry. (n $\geq$ 6, with 150–200 spheroids formed for each experiment per treatment group, ***$P \ll$ .001, *$P \ll$ .05, one-way ANOVA).
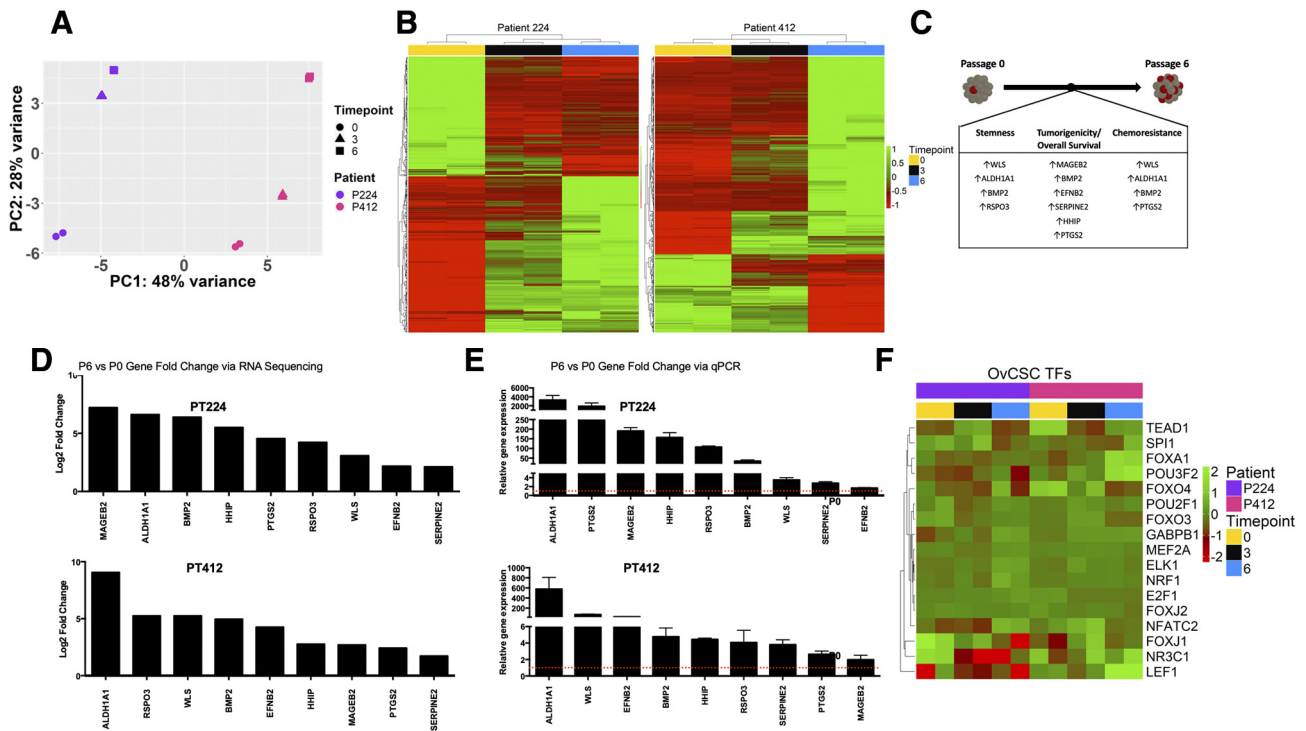

Figure 7. Stem-related pathways are enriched in late-passage spheroids. **A)** Principal component analysis demonstrated emerging differences in Pt224 and Pt412 samples as they proceeded through serial passages P0, P3 and P6; **B)** Heatmaps denoting changes in RNA-Seq between P0, P3 and P6 in Pt224 and Pt412 samples; **C)** Gene signature establishing the stemness, tumorigenicity and chemoresistance of serially passaged spheroids derived from common upregulated genes between both patient samples; **D)** Waterfall plots generated from RNA-Seq analysis of common upregulated genes in P0 *Vs.* P6 for Pt224 and Pt412; **E)** qPCR confirmation of genes from P0 *Vs.* P6 upregulated by RNA-Seq, included in the gene signature; **F)** Heatmap of expression levels of transcription factors commonly implicated in ovarian cancer stem cell maintenance.
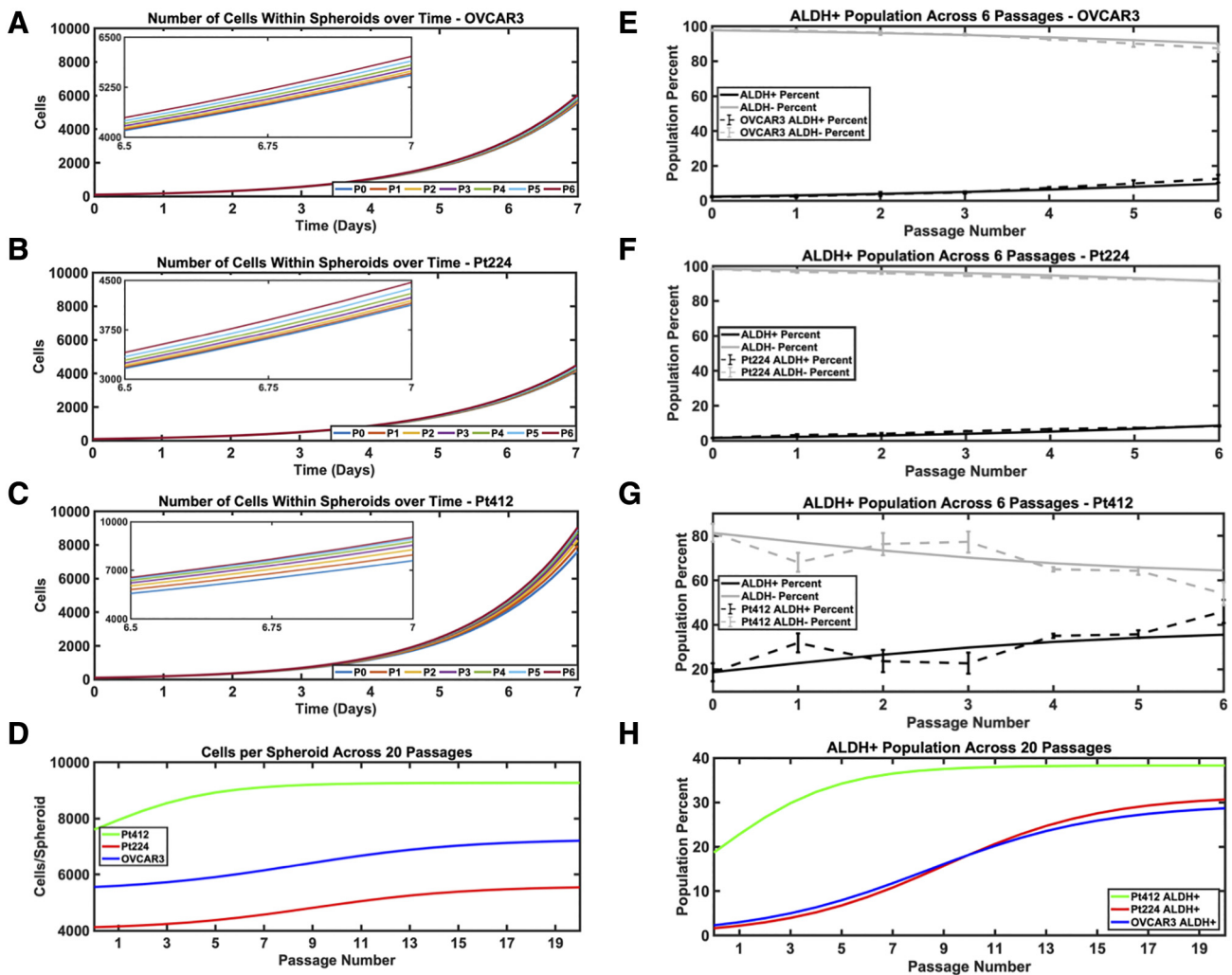
Figure 8. Mathematical modeling of 3D engineered serial passaging. Spheroid growth over the course of 7 days for each passage with the **A**) OVCAR3, **B**) Pt224, and **C**) Pt412. Insets illustrate increase in cell numbers per spheroid across passages from day 6.5 to 7. Emergence of ALDH+ population across 6 passages in the **E**) OVCAR3, **F**) Pt224, and **G**) Pt412. Experimental values are plotted as dotted lines with the standard error of the mean at each passage. **D**) Cells per spheroid and **H**) ALDH percentage simulated over 20 passages for OVCAR3 (blue), Pt224 (red), and Pt412 (green) spheroids.

contributing to relapse and tumor progression [65,66]. Therefore, in this study, we engineered an *in vitro* model that probes development of chemoresistance within a CSC-context. Traditional monolayer models of chemoresistance neither recapitulate the 3D cell–cell interactive microenvironment, nor are they comparable to chemoresistance observed in the clinic [67] [5]. A variety of traditional chemoresistance models also do not address the CSC context. Since the CSC phenotype is notoriously heterogeneous and unstable in 2D monolayer cultures, serial passages in xenografts are performed to study tumor initiating traits and CSC characteristics in serous ovarian cancer [65,68,69]. Genetically engineered mouse models and patient-derived xenografts, although more representative of primary disease, are expensive to establish and perform routinely [70–72]. For these reasons, 3D spheroid and organoid models are used for preclinical drug screening *in vitro* to bridge the gap between 2D monolayer cell culture and xenografts [22,23,73,74]. In our current serially passaged spheroid model, we demonstrate the combined evolution of chemoresistance along with CSC traits *in vitro* – mimicking the progression of recurrent malignant ovarian carcinoma. We address the

challenge that *in vitro* models of recurrence must mimic the complexity and heterogeneity of *in vivo* tumors and provide the longevity needed to capture tumor dormancy following chemotherapy.

We observe that cells placed in the 3D spheroid culture and taken through serial passaging, enriches for CSCs, evidenced by the increasing expression of ALDH through the passages. Our observation of 3D enrichment of the CSC marker, ALDH, is corroborated by increased expression of ALDH1A1 as per RNA-Seq and qRT-PCR, which also showed increased stemness, chemoresistance, and tumorigenicity signatures. This is in line with other reports in various cancers including breast cancers, where enrichment of CSC traits are observed in non-adherent 3D culture systems [75,76]. The increasing ALDH expression with increasing serial passage is correlated with increased proliferative rates of ALDH+ cells, compared to ALDH- cells. Similar to this phenomenon observed by us, Alvero et al. also reported that serially passaging CD44+ epithelial ovarian cancer CSCs triggered a "repair/proliferation" signal, where the process of proliferation by non-stem CD44- cells

derived from a quicker differentiation of CD44+ cells was heightened [20]. Increasing growth rates for serial passaged xenografts were also reported in colorectal tumors, where later generations had higher growth rates compared to earlier generations of xenografted tumors [21]. Moreover, the inconsistent expression of CSC markers in 2D passaging validates the use of our 3D serial passaging model, which produces more consistent and predictable increases in expression of CSC markers with serial passaging.

In this model, we also report that with increasing ALDH+ populations with serial passage, we observe an increasing chemoresistance to conventional platinum-based therapy, and an increased sensitization to Compound 673A, an ALDH targeting compound. We have previously reported that Compound 673A targets the ALDH positive population in patient derived CSC spheroids, and reduces ALDH expression and activity in these spheroids [24]. The increase in chemoresistance to cisplatin is not surprising, given that several reports suggest the strong correlation of the presence of ALDH to chemoresistance in clinical cohorts, as well as, in *in vitro* models and patient derived xenografts in ovarian and other cancers [6,77–79]. Clinically, chemoresistance develops despite initial chemosensitivity in ovarian cancer. Excluding the transition from 2D to P0 3D spheroids, subsequent 3D passaging from P1 onwards resulting in increasing chemoresistance is thereby not surprising and putatively mirrors clinical observations in ovarian cancer.

Similar to reports by Hu et al. [80] where increased tumor burden was observed when side population CSCs were injected into mice, compared to non-side population cells, we observe that injection of spheroids from P6 or P3 (which are significantly more enriched in CSCs) demonstrate a higher tumor burden when compared to spheroids injected from P0, in line with several reports of higher tumor initiating abilities in ALDH+ cells compared to ALDH- cells in murine xenograft models [6,77,81]. Thus, our model was successfully able to enhance tumorigenicity as well. In fact, at late passage (P6) we observed significantly higher estimated cancer stem cell frequency as compared to early passage (P0). This increase in the CSC frequency at late passage was also correlated with earlier tumor establishment and greater tumor burden. Moreover, in comparison with serial passaging in PDXs, our model demonstrates higher efficiency, low cost, low latency, low time commitment, as well as, ability to test numerous patient derived tumors for personalized diagnostics and therapeutics. When considering the clinical utility of this model, it is important to note that while the model in this work is presented over 6 passages, the early passages could be utilized to direct initial therapies, with treatment adjustments being made later based on subsequent passages. Furthermore, with more clinical validation, our mathematical model could be used to predict emergence of CSC phenotypes based only on data from P0 and P1, which could then be used to inform treatment strategies on a much shorter time frame than PDX models.

The validity of our results showing increased stemness, chemoresistance, and tumorigenicity using our model is validated by our RNA-sequencing and qRT-PCR results from P0, P3, and P6 spheroids. In addition to clear changes in gene expression with passaging, we also report a new gene signature of upregulated genes binned into *stemness (WLS, ALDH1A1, BMP2, RSPO3), tumorigenicity (MAGEB2, BMP2, EFNB2, SERPINE2, HHIP, PTGS2),* and *chemoresistance (WLS, ALDA1A1, BMP2, PTGS2)* based on current reports in the cancer literature. Interestingly, *ALDH1A1* was among the top two commonly upregulated genes in both patient samples

regardless of quantification metric. This likely indicates high involvement of ALDH1A1 in stem cell enrichment and increased platinum resistance observed with serial passaging. Furthermore, this finding helps to explain the increased sensitivity to ALHD inhibitor observed with passaging, and lends credence to the use of Compound 673A to treat platinum refractory ovarian cancer.

Our sequencing data also revealed upregulation of two transcription factors, *FOXA1* and *LEF1*, that had previously been associated with ovarian CSCs [36]. Interestingly, these two factors were only found to be significantly upregulated in the Pt412 sample. This difference between Pt224 and Pt412 may be due to the different stage and history of each sample (ascites *vs* abdominal metastasis) as well as the greater increase in ALDH+ OvCSCs in Pt412 spheroids compared to Pt224 spheroids.

As a whole, given the results from our model and previous findings in the literature, we believe that the gene signatures presented by serially passaged P6 spheroids *in vitro* are extremely representative of a clinically malignant, chemoresistant disease portending poor prognosis. It is important to note that while some genes upregulated in our P6 spheroids, such as *BMP2* [38,43,82] and *SERPINE2* [49,55] can be associated with pro- or anti-malignant features in different cancers, their upregulation in our P6 spheroids implicates them in malignant features of ovarian cancer. That said, future studies should further investigate the role of these gene signatures in ovarian cancer and development of chemoresistance with more patient samples and functional assessments of each gene.

Concurrent with our *in vitro* data, the mathematical model demonstrates increased CSC proportions and proliferative capacity in a patient-specific manner over six passages, mimicking the increased tumorigenicity of CSCs. Our model additionally demonstrates CSC-driven tumor development consistent with the CSC hypothesis [29,38]. While our model mimics increased cells per spheroid over 6 passages, the simulated fold increase is significantly lower than that determined experimentally. This discrepancy can be attributed to the simplicity of the model, which will be made increasingly more robust with additional biological considerations, such as dedifferentiation [83], successive decrease in progenitor proliferation capacity [28], or the stratified proliferative, quiescent, and necrotic regions that may form within spheroids [84], for example. However, over longer term passaging our model predicts a plateau in cells per spheroid which could represent the development of quiescent and necrotic regions within a spheroid as it grows larger and the inner cores become deprived of nutrients and oxygen [85]. While this cannot be confirmed with our data, it serves as a solid basis for future experimentation. Interestingly, our model also predicts the eventual plateau of CSC populations within spheroids of each sample over the course of 20 passages, which could not be discerned from our experimental data within the six serial passages. This finding supports reports of negative feedback control on CSC populations by non-CSCs when space is limited [86]. In the 20-passage simulation, Pt412 spheroids were shown to reach cell/spheroid and CSC population plateaus much faster than the other two samples. This finding perhaps indicates that Pt412 would be quicker to develop ALDH conferred chemoresistance and relapse as their corresponding spheroids were simulated to reach their putative nutrient and space limitations fastest. Given that Pt412 contains the highest proportion of ALDH+ cells, which are generally more proliferative and chemoresistant [32,87,88], this observation is plausible. Additionally, this interpretation supports our *in vivo* evidence showing that xenograft tumors

generated from Pt412 spheroids reached the tumor size endpoint 1 week faster for P0 and P3 and 2 weeks faster for P6 than tumors generated from Pt224 spheroids. These findings may be indicative of the need for differential treatment strategies for Pt412 and Pt224.

While other mathematical models have been developed to describe tumor growth dynamics and chemoresistance relative to CSC proportion, none have modeled CSC emergence in serial passaging of epithelial ovarian cancer spheroids [27–30,89–91], which can provide easily discernable, experimentally derived parameter-values to enhance biological relevance of the model. Similar to our model, Fornari et al. [28] proposed an experimentally informed system of equations to investigate CSC-driven tumorigenesis and analyze tumor growth dynamics based on CSC population proportions at passage 1, 2, and 3. Analysis of this model was contained within each passage and did not attempt to predict increased CSC populations across passages. Fornari's model, as well as others, solely attempt to model population development within a single growth iteration and do not attempt to predict emergence of increasing CSC populations across iterations [28,29,31] limiting their utility in modeling emergence of CSC-related chemoresistance upon relapse. Lastly, many other mathematical models of tumor recurrence do not take into account the role of cancer stem cells in relapsed tumors and resulting increased chemoresistance [92–94]. Therefore, while simple, our model demonstrates a novel mathematical application by which the development of chemoresistance within epithelial ovarian cancer can be inferred in a patient-specific manner using only data from P0 and P1. Moreover, our math model can be easily adapted to include other experimental parameters that influence CSC evolution, including hypoxia, extracellular matrix biophysical properties, stem cell plasticity, and paracrine interactions with other cell types in the TME.

Through these studies, we report an *in vitro* spheroid model that generates reproducible spheroids and results, takes a relatively short period of time to develop, more accurately addresses *in situ* chemoresistance development, and could be further used to examine the development of chemoresistance in the setting of enhanced cancer stem cell populations. This serial passage hanging drop model also incorporates the study of ovarian CSCs, thereby modeling the evolution and emergence of chemoresistance within a micro-tumor with a CSC-context. Since chemoresistance is observed in many ovarian cancer patients after first line chemotherapy, and we observe increased resistance to conventional chemotherapy in serially passaged spheroids, this model is well suited to study the *in situ* emergence of chemoresistance. Using the serial passage spheroid model, widely available -omics approaches can be used to analyze changes at genetic, epigenetic, metabolic and secretome levels, and compare them between parental tumors, chemosensitive and subsequent chemoresistant passages. The evolution of chemoresistance could be related to molecular mechanisms, and the mechanistic roles attributed to key players within the molecular pathways could be further explored *in vitro*. This model has a wide variety of applications in both biomarker discovery, as well as preclinical screening from an evolved chemoresistant tumor standpoint. Apart from the obvious advantage of being physiologically relevant, the serial passage spheroid model recapitulates the existence of CSCs in malignant ascites that aggregate into spheroids to escape anoikis and maintains cellular heterogeneity of patient derived ovarian tumors, which can be utilized to study cellular interactions and their resultant biology in a systematic manner. Lastly, this model could be used as a way to enrich CSCs and chemoresistance within patient derived cells, and ultimately examine better treatment options for these patients. Therefore, we present a newly engineered 3D ovarian cancer model to discern the underpinnings of chemoresistance development and role of ovarian CSCs in this process.

Conflict of Interests

The authors have no conflict of interest to declare.

Appendix A. Supplementary data

Supplementary data to this article can be found online at https://doi.org/10.1016/j.neo.2019.06.005.

References

[1] http://seer.cancer.gov/statfacts/html/ovary.html . Editor (ed)^(eds): City.

[2] Piccart MJ, Bertelsen K, James K, Cassidy J, Mangioni C, Simonsen E, Stuart G, Kaye S, Vergote I, and Blom R, et al (2000). Randomized intergroup trial of cisplatin-paclitaxel versus cisplatin-cyclophosphamide in women with advanced epithelial ovarian cancer: three-year results. *J Natl Cancer Inst* **92**, 699–708.

[3] Kemp Z and Ledermann J (2013). Update on first-line treatment of advanced ovarian carcinoma. *Int J Women's Health* **5**, 45–51.

[4] du Bois A, Neijt JP, and Thigpen JT (1999). First line chemotherapy with carboplatin plus paclitaxel in advanced ovarian cancer—a new standard of care? *Ann Oncol* **10**(Suppl 1), 35–41.

[5] Agarwal R and Kaye SB (2003). Ovarian cancer: strategies for overcoming resistance to chemotherapy. *Nat Rev Cancer* **3**, 502–516.

[6] Silva IA, Bai S, McLean K, Yang K, Griffith K, Thomas D, Ginestier C, Johnston C, Kueck A, and Reynolds RK, et al (2011). Aldehyde dehydrogenase in combination with CD133 defines angiogenic ovarian cancer stem cells that portend poor patient survival. *Cancer Res* **71**, 3991–4001.

[7] Wang YC, Yo YT, Lee HY, Liao YP, Chao TK, Su PH, and Lai HC (2012). ALDH1-bright epithelial ovarian cancer cells are associated with CD44, drug resistance, and poor clinical outcome. *Am J Pathol* **180**, 1159–1169.

[8] Winer I, Wang S, Lee YE, Fan W, Gong Y, Burgos-Ojeda D, Spahlinger G, Kopelman R, and Buckanovich RJ (2010). F3-targeted cisplatin-hydrogel nanoparticles as an effective therapeutic that targets both murine and human ovarian tumor endothelial cells in vivo. *Cancer Res* **70**, 8674–8683.

[9] Yamada KM and Cukierman E (2007). Modeling tissue morphogenesis and cancer in 3D. *Cell* **130**, 601–610.

[10] Pardal R, Clarke MF, and Morrison SJ (2003). Applying the principles of stem-cell biology to cancer. *Nat Rev Cancer* **3**, 895–902.

[11] Reya T, Morrison SJ, Clarke MF, and Weissman IL (2001). Stem cells, cancer, and cancer stem cells. *Nature* **414**, 105–111.

[12] Konstantinopoulos PA, Spentzos D, and Cannistra SA (2008). Gene-expression profiling in epithelial ovarian cancer. *Nat Clin Pract Oncol* **5**, 577–587.

[13] Hickman JA, Graeser R, de Hoogt R, Vidic S, Brito C, Gutekunst M, van der Kuip H, and Consortium IP (2014). Three-dimensional models of cancer for pharmacology and cancer cell biology: capturing tumor complexity in vitro/ex vivo. *Biotechnol J* **9**, 1115–1128.

[14] Lengyel E, Burdette JE, Kenny HA, Matei D, Pilrose J, Haluska P, Nephew KP, Hales DB, and Stack MS (2014). Epithelial ovarian cancer experimental models. *Oncogene* **33**, 3619–3633.

[15] Cunnea P and Stronach EA (2014). Modeling platinum sensitive and resistant high-grade serous ovarian cancer: development and applications of experimental systems. *Front Oncol* **4**, 81.

[16] Harrison H, Farnie G, Howell SJ, Rock RE, Stylianou S, Brennan KR, Bundred NJ, and Clarke RB (2010). Regulation of breast cancer stem cell activity by signaling through the Notch4 receptor. *Cancer Res* **70**, 709–718.

[17] Nagata S, Hirano K, Kanemori M, Sun LT, and Tada T (2012). Self-renewal and pluripotency acquired through somatic reprogramming to human cancer stem cells. *PLoS One* **7**e48699.

[18] Wu C and Alman BA (2008). Side population cells in human cancers. *Cancer Lett* **268**, 1–9.

[19] Louie E, Nik S, Chen JS, Schmidt M, Song B, Pacson C, Chen XF, Park S, Ju J, and Chen EI (2010). Identification of a stem-like cell population by exposing metastatic breast cancer cell lines to repetitive cycles of hypoxia and reoxygenation. *Breast Cancer Res* **12**, R94.

[20] Alvero AB, Chen R, Fu HH, Montagna M, Schwartz PE, Rutherford T, Silasi DA, Steffensen KD, Waldstrom M, and Visintin I, et al (2009). Molecular phenotyping of human ovarian cancer stem cells unravels the mechanisms for repair and chemoresistance. *Cell Cycle* **8**, 158–166.

[21] Houghton JA and Taylor DM (1978). Growth characteristics of human colorectal tumours during serial passage in immune-deprived mice. *Br J Cancer* **37**, 213–223.

[22] Raghavan S, Mehta P, Horst EN, Ward MR, Rowley KR, Mehta G, Raghavan S, Mehta P, Horst EN, and Ward MR, et al (2016). Comparative analysis of tumor spheroid generation techniques for differential in vitro drug toxicity. *Oncotarget* **7**, 16948–16961.

[23] Raghavan S, Ward MR, Rowley KR, Wold RM, Takayama S, Buckanovich RJ, and Mehta G (2015). Formation of stable small cell number three-dimensional ovarian cancer spheroids using hanging drop arrays for preclinical drug sensitivity assays. *Gynecol Oncol* **138**(1), 181–189.

[24] Raghavan S, Mehta P, Ward MR, Bregenzer ME, Fleck EMA, Tan L, McLean K, Buckanovich RJ, and Mehta G (2017). Personalized medicine-based approach to model patterns of chemoresistance and tumor recurrence using ovarian cancer stem cell spheroids. *Clin Cancer Res* **23**, 6934–6945.

[25] Mehta P, Novak C, Raghavan S, Ward M, and Mehta G (2018). In: Papaccio G, Desiderio V, editors. Self-Renewal and CSCs In Vitro Enrichment: Growth as Floating Spheres. New York, NY: Springer New York; 2018. p. 61–75.

[26] Mehta G, Hsiao AY, Ingram M, Luker GD, and Takayama S (2012). Opportunities and challenges for use of tumor spheroids as models to test drug delivery and efficacy. *J Control Release* **164**(2), 192–204.

[27] Loessner D, Flegg JA, Byrne HM, Clements JA, and Hutmacher DW (2013). Growth of confined cancer spheroids: a combined experimental and mathematical modelling approach. *Integr Biol (Camb)* **5**, 597–605.

[28] Fornari C, Beccuti M, Lanzardo S, Conti L, Balbo G, Cavallo F, Calogero RA, and Cordero F (2014). A mathematical-biological joint effort to investigate the tumor-initiating ability of Cancer Stem Cells. *PLoS One* **9**e106193.

[29] Molina-Pena R and Alvarez MM (2012). A simple mathematical model based on the cancer stem cell hypothesis suggests kinetic commonalities in solid tumor growth. *PLoS One* **7**e26233.

[30] Weekes SL, Barker B, Bober S, Cisneros K, Cline J, Thompson A, Hlatky L, Hahnfeldt P, and Enderling H (2014). A multicompartment mathematical model of cancer stem cell-driven tumor growth dynamics. *Bull Math Biol* **76**, 1762–1782.

[31] Pearson AT, Ingram P, Bai S, O'Hayer P, Chung J, Yoon E, Jackson T, and Buckanovich RJ (2017). Sampling from single-cell observations to predict tumor cell growth in-vitro and in-vivo. *Oncotarget* **8**, 111176–111189.

[32] Chefetz I, Grimley E, Yang K, Hong L, Vinogradova EV, Suciu R, Kovalenko I, Karnak D, Morgan CA, and Chtcherbinine M, et al (2019). A Pan-ALDH1A inhibitor induces necroptosis in ovarian cancer stem-like cells. *Cell Rep* **26**, 3061–3075.e3066.

[33] Love MI, Huber W, and Anders S (2014). Moderated estimation of fold change and dispersion for RNA-seq data with DESeq2. *Genome Biol* **15**, 550.

[34] Durinck S, Spellman PT, Birney E, and Huber W (2009). Mapping identifiers for the integration of genomic datasets with the R/Bioconductor package biomaRt. *Nat Protoc* **4**, 1184–1191.

[35] Gu Z, Eils R, and Schlesner M (2016). Complex heatmaps reveal patterns and correlations in multidimensional genomic data. *Bioinformatics* **32**, 2847–2849.

[36] Zhang T, Xu J, Deng S, Zhou F, Li J, Zhang L, Li L, Wang Q-E, and Li F (2018). Core signaling pathways in ovarian cancer stem cell revealed by integrative analysis of multi-marker genomics data. *PLoS One* **13**e0196351.

[37] Tomasetti C and Levy D (2010). Role of symmetric and asymmetric division of stem cells in developing drug resistance. *Proc Natl Acad Sci U S A* **107**, 16766–16771.

[38] Choi YJ, Ingram PN, Yang K, Coffman L, Iyengar M, Bai S, Thomas DG, Yoon E, and Buckanovich RJ (2015). Identifying an ovarian cancer cell hierarchy regulated by bone morphogenetic protein 2. *Proc Natl Acad Sci U S A* **112**, E6882-6888.

[39] Stewart J, James J, McCluggage GW, McQuaid S, Arthur K, Boyle D, Mullan P, McArt D, Yan B, and Irwin G, et al (2015). Analysis of wntless (WLS) expression in gastric, ovarian, and breast cancers reveals a strong association with HER2 overexpression. *Mod Pathol* **28**, 428–436.

[40] Valkenburg KC, Graveel CR, Zylstra-Diegel CR, Zhong Z, and Williams BO (2011). Wnt/β-catenin signaling in normal and cancer stem cells. *Cancers* **3**, 2050–2079.

[41] Kryczek I, Liu S, Roh M, Vatan L, Szeliga W, Wei S, Banerjee M, Mao Y, Kotarski J, and Wicha MS, et al (2012). Expression of aldehyde dehydrogenase and CD133 defines ovarian cancer stem cells. *Int J Cancer* **130**, 29–39.

[42] Meng E, Mitra A, Tripathi K, Finan MA, Scalici J, McClellan S, Madeira da Silva L, Reed E, Shevde LA, and Palle K, et al (2014). ALDH1A1 maintains ovarian cancer stem cell-like properties by altered regulation of cell cycle checkpoint and DNA repair network signaling. *PLoS One* **9**e107142.

[43] Huang P, Chen A, He W, Li Z, Zhang G, Liu Z, Liu G, Liu X, He S, and Xiao G, et al (2017). BMP-2 induces EMT and breast cancer stemness through Rb and CD44. *Cell Death Dis* **3**, 17039.

[44] De Sousa e Melo F and Vermeulen L (2016). Wnt signaling in cancer stem cell biology. *Cancers* **8**, 60.

[45] Vangipuram SD, Buck SA, and Lyman WD (2012). Wnt pathway activity confers chemoresistance to cancer stem-like cells in a neuroblastoma cell line. *Tumour Biol* **33**, 2173–2183.

[46] Peche LY, Ladelfa MF, Toledo MF, Mano M, Laiseca JE, Schneider C, and Monte M (2015). Human MageB2 protein expression enhances E2F transcriptional activity, Cell Proliferation, and Resistance to Ribotoxic Stress. *J Biol Chem* **290**, 29652–29662.

[47] Weon JL and Potts PR (2015). The MAGE protein family and cancer. *Curr Opin Cell Biol* **37**, 1–8.

[48] Zhang Y, Zhang R, Ding X, and Ai K (2018). EFNB2 acts as the target of miR-557 to facilitate cell proliferation, migration and invasion in pancreatic ductal adenocarcinoma by bioinformatics analysis and verification. *Am J Transl Res* **10**, 3514–3528.

[49] Bergeron S, Lemieux E, Durand V, Cagnol S, Carrier JC, Lussier JG, Boucher M-J, and Rivard N (2010). The serine protease inhibitor serpinE2 is a novel target of ERK signaling involved in human colorectal tumorigenesis. *Mol Cancer* **9**, 271.

[50] Buchholz M, Biebl A, Neeβe A, Wagner M, Iwamura T, Leder G, Adler G, and Gress TM (2003). SERPINE2 (Protease Nexin I) promotes extracellular matrix production and local invasion of pancreatic tumors in vivo. *Cancer Res* **63**, 4945–4951.

[51] Stępień T, Brożyna M, Kuzdak K, Motylewska E, Komorowski J, Stępień H, and Ławnicka H (2017). Elevated concentrations of SERPINE2/protease nexin-1 and secretory leukocyte protease inhibitor in the serum of patients with papillary thyroid cancer; 2017 . Editor (ed)^(eds): City.

[52] Vaillant C, Valdivieso P, Nuciforo S, Kool M, Schwarzentruber-Schauerte A, Méreau H, Cabuy E, Lobrinus JA, Pfister S, and Zuniga A, et al (2015). Serpine2/PN-1 Is Required for Proliferative Expansion of Pre-Neoplastic Lesions and Malignant Progression to Medulloblastoma. *PLoS One* **10**.

[53] Yang Y, Xin X, Fu X, and Xu D (2018). Expression pattern of human SERPINE2 in a variety of human tumors. *Oncol Lett* **15**, 4523–4530.

[54] Chen Q, Gao G, and Luo S (2013). Hedgehog signaling pathway and ovarian cancer. *Chin J Cancer Res* **25**, 346–353.

[55] Holtz AM, Griffiths SC, Davis SJ, Bishop B, Siebold C, and Allen BL (2015). Secreted HHIP1 interacts with heparan sulfate and regulates Hedgehog ligand localization and function. *J Cell Biol* **209**, 739–758.

[56] Szkandera J, Kiesslich T, Haybaeck J, Gerger A, and Pichler M (2013). Hedgehog signaling pathway in ovarian cancer. *Int J Mol Sci* **14**, 1179–1196.

[57] Pang LY, Hurst EA, and Argyle DJ (2016). Cyclooxygenase-2: A role in cancer stem cell survival and repopulation of cancer cells during therapy; 2016 . Editor (ed)^(eds): City.

[58] Sun H, Zhang X, Sun D, Jia X, Xu L, Qiao Y, and Jin Y (2017). COX-2 expression in ovarian cancer: an updated meta-analysis. *Oncotarget* **8**, 88152–88162.

[59] Uddin S, Ahmed M, Hussain A, Assad L, Al-Dayel F, Bavi P, Al-Kuraya KS, and Munkarah A (2010). Cyclooxygenase-2 inhibition inhibits PI3K/AKT kinase activity in epithelial ovarian cancer. *Int J Cancer* **126**, 382–394.

[60] Wang D, Xia D, and DuBois RN (2011). The crosstalk of PTGS2 and EGF signaling pathways in colorectal cancer. *Cancers* **3**, 3894–3908.

[61] Mohammed MK, Shao C, Wang J, Wei Q, Wang X, Collier Z, Tang S, Liu H, Zhang F, and Huang J, et al (2016). Wnt/β-catenin signaling plays an ever-expanding role in stem cell self-renewal, tumorigenesis and cancer chemoresistance. *Genes Dis* **3**, 11–40.

[62] Clark DW and Palle K (2016). Aldehyde dehydrogenases in cancer stem cells: potential as therapeutic targets. *Ann Transl Med* **4**.

[63] Croker AK, Rodriguez-Torres M, Xia Y, Pardhan S, Leong HS, Lewis JD, and Allan AL (2017). Differential functional roles of ALDH1A1 and ALDH1A3 in mediating metastatic behavior and therapy resistance of human breast cancer cells. *Int J Mol Sci* **18**.

[64] Xu H, Lin F, Wang Z, Yang L, Meng J, Ou Z, Shao Z, Di G, and Yang G (2018). CXCR2 promotes breast cancer metastasis and chemoresistance via suppression of AKT1 and activation of COX2. *Cancer Lett* **412**, 69–80.

[65] Bapat SA, Mali AM, Koppikar CB, and Kurrey NK (2005). Stem and progenitor-like cells contribute to the aggressive behavior of human epithelial ovarian cancer. *Cancer Res* **65**, 3025–3029.

[66] Steffensen KD, Alvero AB, Yang Y, Waldstrom M, Hui P, Holmberg JC, Silasi DA, Jakobsen A, Rutherford T, and Mor G (2011). Prevalence of epithelial ovarian cancer stem cells correlates with recurrence in early-stage ovarian cancer. *J Oncol* **2011**, 620523.

[67] Okamoto A, Nikaido T, Ochiai K, Takakura S, Saito M, Aoki Y, Ishii N, Yanaihara N, Yamada K, and Takikawa O, et al (2005). Indoleamine 2,3-dioxygenase serves as a marker of poor prognosis in gene expression profiles of serous ovarian cancer cells. *Clin Cancer Res* **11**, 6030–6039.

[68] Curley MD, Therrien VA, Cummings CL, Sergent PA, Koulouris CR, Friel AM, Roberts DJ, Seiden MV, Scadden DT, and Rueda BR, et al (2009). CD133 expression defines a tumor initiating cell population in primary human ovarian cancer. *Stem Cells* **27**, 2875–2883.

[69] Stewart JM, Shaw PA, Gedye C, Bernardini MQ, Neel BG, and Ailles LE (2011). Phenotypic heterogeneity and instability of human ovarian tumor-initiating cells. *Proc Natl Acad Sci U S A* **108**, 6468–6473.

[70] Ricci F, Broggini M, and Damia G (2013). Revisiting ovarian cancer preclinical models: implications for a better management of the disease. *Cancer Treat Rev* **39**, 561–568.

[71] Helland O, Popa M, Vintermyr OK, Molven A, Gjertsen BT, Bjorge L, and McCormack E (2014). First in-mouse development and application of a surgically relevant xenograft model of ovarian carcinoma. *PLoS One* **9**e89527.

[72] Dobbin ZC, Katre AA, Steg AD, Erickson BK, Shah MM, Alvarez RD, Conner MG, Schneider D, Chen D, and Landen CN (2014). Using heterogeneity of the patient-derived xenograft model to identify the chemoresistant population in ovarian cancer. *Oncotarget* **5**, 8750–8764.

[73] Friedrich J, Seidel C, Ebner R, and Kunz-Schughart LA (2009). Spheroid-based drug screen: considerations and practical approach. *Nat Protoc* **4**, 309–324.

[74] Hirschhaeuser F, Menne H, Dittfeld C, West J, Mueller-Klieser W, and Kunz-Schughart LA (2010). Multicellular tumor spheroids: an underestimated tool is catching up again. *J Biotechnol* **148**, 3–15.

[75] Dontu G, Abdallah WM, Foley JM, Jackson KW, Clarke MF, Kawamura MJ, and Wicha MS (2003). In vitro propagation and transcriptional profiling of human mammary stem/progenitor cells. *Genes Dev* **17**, 1253–1270.

[76] Chen SF, Chang YC, Nieh S, Liu CL, Yang CY, and Lin YS (2012). Nonadhesive culture system as a model of rapid sphere formation with cancer stem cell properties. *PLoS One* **7**e31864.

[77] Landen Jr CN, Goodman B, Katre AA, Steg AD, Nick AM, Stone RL, Miller LD, Mejia PV, Jennings NB, and Gershenson DM, et al (2010). Targeting aldehyde dehydrogenase cancer stem cells in ovarian cancer. *Mol Cancer Ther* **9**, 3186–3199.

[78] Cojoc M, Peitzsch C, Kurth I, Trautmann F, Kunz-Schughart LA, Telegeev GD, Stakhovsky EA, Walker JR, Simin K, and Lyle S, et al (2015). Aldehyde dehydrogenase is regulated by beta-catenin/TCF and promotes radioresistance in prostate cancer progenitor cells. *Cancer Res* **75**, 1482–1494.

[79] Tanei T, Morimoto K, Shimazu K, Kim SJ, Tanji Y, Taguchi T, Tamaki Y, and Noguchi S (2009). Association of breast cancer stem cells identified by aldehyde dehydrogenase 1 expression with resistance to sequential Paclitaxel and epirubicin-based chemotherapy for breast cancers. *Clin Cancer Res* **15**, 4234–4241.

[80] Hu L, McArthur C, and Jaffe RB (2010). Ovarian cancer stem-like side-population cells are tumourigenic and chemoresistant. *Br J Cancer* **102**, 1276–1283.

[81] Lin L, Liu A, Peng Z, Lin HJ, Li PK, Li C, and Lin J (2011). STAT3 is necessary for proliferation and survival in colon cancer-initiating cells. *Cancer Res* **71**, 7226–7237.

[82] Wang L, Park P, Zhang H, La Marca F, Claeson A, Valdivia J, and Lin C-Y (2011). BMP-2 inhibits the tumorigenicity of cancer stem cells in human osteosarcoma OS99-1 cell line. *Cancer Biol Ther* **11**, 457–463.

[83] Dhawan A, Madani Tonekaboni SA, Taube JH, Hu S, Sphyris N, Mani SA, and Kohandel M (2016). Mathematical modelling of phenotypic plasticity and conversion to a stem-cell state under hypoxia. *Sci Rep* **6**, 18074.

[84] Wallace DI and Guo X (2013). Properties of tumor spheroid growth exhibited by simple mathematical models. *Front Oncol* **3**, 51.

[85] Däster S, Amatruda N, Calabrese D, Ivanek R, Turrini E, Droeser RA, Zajac P, Fimognari C, Spagnoli GC, and Iezzi G, et al (2016). Induction of hypoxia and necrosis in multicellular tumor spheroids is associated with resistance to chemotherapy treatment. *Oncotarget* **8**, 1725–1736.

[86] Enderling H (2015). Cancer stem cells: small subpopulation or evolving fraction? *Integr Biol (Camb)* **7**, 14–23.

[87] Bai S, Ingram P, Chen Y-C, Deng N, Pearson A, Niknafs Y, O'Hayer P, Wang Y, Zhang Z-Y, and Boscolo E, et al (2016). EGFL6 regulates the asymmetric division, maintenance and metastasis of ALDH+ ovarian cancer cells. *Cancer Res* **76**, 6396–6409.

[88] Jia L-Y, Xia H-L, Chen Z-D, Compton C, Bucur H, Sawant DA, Rankin GO, Li B, Tu Y-Y, and Chen YC (2018). Anti-proliferation effect of theasaponin E1 on the ALDH-positive ovarian cancer stem-like cells. *Molecules* **23**.

[89] Foo J and Michor F (2010). Evolution of resistance to anti-cancer therapy during general dosing schedules. *J Theor Biol* **263**, 179–188.

[90] Nazari F, Pearson AT, Nor JE, and Jackson TL (2018). A mathematical model for IL-6-mediated, stem cell driven tumor growth and targeted treatment. *PLoS Comput Biol* **14**e1005920.

[91] Werner B, Scott JG, Sottoriva A, Anderson AR, Traulsen A, and Altrock PM (2016). The cancer stem cell fraction in hierarchically organized tumors can be estimated using mathematical modeling and patient-specific treatment trajectories. *Cancer Res* **76**, 1705–1713.

[92] Enderling H, Chaplain MA, Anderson AR, and Vaidya JS (2007). A mathematical model of breast cancer development, local treatment and recurrence. *J Theor Biol* **246**, 245–259.

[93] Parra-Guillen ZP, Berraondo P, Grenier E, Ribba B, and Troconiz IF (2013). Mathematical model approach to describe tumour response in mice after vaccine administration and its applicability to immune-stimulatory cytokine-based strategies. *AAPS J* **15**, 797–807.

[94] Xie X, Hu Y, Jing C, Luo S, Lv Y, Yang H, Li L, Chen H, Lin W, and Zheng W (2017). A comprehensive model for predicting recurrence and survival in cases of chinese postoperative invasive breast cancer. *Asian Pac J Cancer Prev* **18**, 727–733.